Plasmon-Assisted Broadband All-Optical Control of Highly Intense Femtosecond Laser by Weak Continuous-Wave Laser

Chi Zhang, Hao Wu, Yanming Xu, Jinlong Xu,* Zhong Yan,* Yonghong Hu, Zhenda Xie,* and Shining Zhu

Dynamically manipulating highly intense ultrafast pulses by optical modulators is extremely useful for strong-field physics. However, the manipulation has been severely restricted by the fundamental drawbacks of most modulators such as the low laser damage threshold and high energy consumption. Here, the implementation of an all-optical modulator on femtosecond lasers up to 10^{11} W cm^{-2} covering wavelengths from 1.6 to 2.3 µm is demonstrated; the modulator is controlled by a weak continuous-wave laser ($\approx 10^3$ W cm^{-2}) based on the prominent plasmon-assisted thermo-optic nonlinearity of suspended antimonene quantum dots (AQDs). The strong localization of the surface plasmon of the AQDs contributes a tremendous effective nonlinear refractive index ($n_2 \approx 10^{-5}$ cm^2 W^{-1}) under weak light excitation, modulating the optical phase of copropagating intense lasers, and realizing robust "ON/OFF" alterations. It is also verified that the thermo-optical effect occurs at a fast speed of ≈ 240 ps in this nanomaterial system. The findings provide new insight for exploiting the potential of plasmonic nonlinearities of nanomaterials, which offers a pragmatic and extensible solution to the urgent demand for manipulating and optical limiting of strong field physics in further nanophotonic platforms.

1. Introduction

Currently, commercial ultrafast lasers can achieve high intensities exceeding 10^{11} W cm^{-2}, providing exciting opportunities in strong-field physics investigations. For realistic applications, it

is urgent to develop the dynamic manipulation of the fundamental properties of high-intensity lasers, such as the phase, frequency, and amplitude,[1] where optical modulators are essential control components. Electro-optic modulators (EOMs) have played a primary role in current communication systems, but they suffer from two major weaknesses. One weakness is the trade-off between the modulation speed and on/off switch ratio owing to the electron–hole dynamics in the gate capacitance. The other weakness is the low optical damage threshold. Commercially advanced EOMs made of liquid crystals and MgO-doped LiNbO$_3$ can only bear maximum light intensities of 8 and 400 W cm^{-2}, respectively, which are far below the general intensities of ultrafast lasers.[2] In contrast, by means of light–matter interactions to tune the refractive index of optical materials, the vexing trade-off can be avoided in an all-optical modulator (AOM),[3] and the designs of a plasmon-based AOM for femtosecond pulses exceeding TW cm^{-2} have been theoretically proposed.[4] However, the intensities of the control laser beams are required to be comparable to or much stronger than the signals, resulting in high energy consumption during intense laser modulation.

Recently, low-dimensional nanomaterials (e.g., graphene, MoS$_2$, black phosphorus) have shown a surprisingly large nonlinear refractive index n_2 (10^{-8}–10^{-5} cm^2 W^{-1}),[5] several orders of magnitude larger than that of silicon ($\approx 10^{-14}$ cm^2 W^{-1})[6] and silica ($\approx 10^{-16}$ cm^2 W^{-1}).[6] Furthermore, spatial self-phase modulation (SSPM)[5] and spatial cross-phase modulation (SXPM) effects between two copropagating beams have been demonstrated as an effective way to realize a novel AOM.[7] Besides, a special hybrid structure has been successfully proposed to realize the nonreciprocal light propagation in the nonlinear photonic diode, by combining the strong SSPM effect of 2D Te (or graphdiyne) with other reverse saturable absorption nanomaterials such as SnS$_2$, which provides a new device for all-optical signal processing.[8] Recent studies reported antimony, a new number of group-VA 2D materials, for the use of ultrafast laser generation and ultrasensitive detection of miRNA.[9] In addition, antimonene quantum dots (AQDs) have shown

C. Zhang, H. Wu, Y. M. Xu, Dr. J. L. Xu, Prof. Z. D. Xie, Prof. S. N. Zhu
National Laboratory of Solid-State Microstructure
Nanjing University
Nanjing 210093, China
E-mail: longno.2@163.com; xiezhenda@nju.edu.cn
Prof. Z. Yan
College of Materials Science and Engineering
Nanjing University of Science and Technology
Nanjing 210094, China
E-mail: zhongyan@njust.edu.cn
Prof. Y. H. Hu
School of Nuclear Technology and Chemistry & Biology
Hubei University of Science and Technology
Xianning 437100, China

ADVANCED
SCIENCE NEWS
www.advancedsciencenews.com

ADVANCED
OPTICAL
MATERIALS
www.advopticalmat.de

remarkable photothermal effects experimentally, with potential applications in effective cancer therapy.[10] Meanwhile, a strong SSPM effect of AQDs suspensions at excitation wavelengths of 532 and 633 nm was observed,[11] suggesting excellent potential in the further design of novel AOMs.

In this work, a weak-control-strong AOM where a weak continuous-wave (CW) laser can manipulate the propagation of broadband strong pulsed lasers in the region from near-infrared (NIR) to mid-infrared (MIR) is elaborately demonstrated, through the efficient plasmon-assisted SXPM effect of suspended AQDs. The signal lasers exhibit wavelengths and intensities as follows: femtosecond lasers ($\approx 10^{11}$ W cm^{-2}) with wavelengths ranging from 1.6 to 2.3 µm, a picosecond laser (10^3 W cm^{-2}) at a wavelength of 3 µm, and a CW laser (34 W cm^{-2}) at a wavelength of 2 µm, and the corresponding intensity ratios between the control and signal lasers are 1:1.5 × 10^8, 1:180, and 1:9.5, respectively. The fast decay of plasmon-induced hot electrons enables highly efficient energy conversion from weak modulation light to a localized solvo-thermal process through a strong localized surface plasmon resonance (LSPR) of nanostructure AQDs, eventually forming a thermal-induced refractive index field (RIF) in the AQD suspension. The pump-probe measurement shows that the RIF has a fast relaxation time of $\approx$240 ps, which rapidly reconfigures the phase distribution of the copropagating strong laser beams from the fundamental mode to diffraction rings, leading to an "ON/OFF" modulation. This AOM is polarization-independent (Figure S7, Supporting Information), convenient for practical applications and can also serve as a self-adapted optical limitation for intense laser. The modulation dynamic can be well simulated with the finite-difference time-domain (FDTD) method. By combining the plasmon-hot effect and optical nonlinearity, this work provides a new platform for the dynamic control and optical limitation of highly intense lasers, which may meet the dramatically increased interest in exploring strong-field physics.

2. Results and Discussion

2.1. Synthesis and Optical Properties of AQDs

The high-yield preparation of AQDs was realized by directly exploiting antimony powder through facile water-bath sonication, as shown in **Figure 1**a (see the Experimental Section and Note S1, Supporting Information, for details). Note that one of the kernels for preparation efficiency was the appropriate choice of the solvent for powders. Compared with a variety of common hypotoxicity solvents, such as acetone, ethyl ethanol, methyl alcohol, methylbenzene, and distilled water, under the same experimental conditions, we found that sonication of Sb in N-methyl-2-pyrrolidinone (NMP) resulted in a much higher yield of uniform nanoparticles (Figure 1b). The reason may be attributed to the matching between the strong surface energy of NMP and the Sb−Sb covalent bond, facilitating the pulling off of Sb atoms easily from the pristine bulk by the interface friction of NMP. Atomic force microscopy (AFM) measurements were carried out to assess the thickness of the AQDs as shown in Figure 1c,d. The typical thickness of the AQDs is in the range of 1.7–3.6 nm. The transmission electron microscopy

(TEM) characterization in Figure S1d,e (Supporting Information) illustrates that size distribution has an average lateral size of 2.7 ± 0.6 nm ($\approx$7 atomic layers[11]). This result is consistent with the AFM results, proving that direct exfoliation in NMP is an appropriate approach for the high-yield synthesis of regular AQDs. Moreover, high-resolution TEM (Figure 1e) shows the arrangement of atomics with a d spacing of 0.21 nm at (110), which is the typical parameter of rhombohedral-phase antimony.[12] The X-ray diffraction (XRD) pattern of AQDs also confirms the unchanged crystal structure of AQDs during the exfoliation process (Figure S1f, Supporting Information). The collected Raman spectra of vibration modes E$_g$ and A$_{1g}$ (Note S1 and Figure S1g, Supporting Information) represent a blueshift after exfoliation from bulk into AQDs, which should be contributed to the long-range Coulombic interlayer interactions or constant shrinkage when decreasing the number of atomic layers.[12b,13] The long-term chemical stability of as-prepared AQDs is confirmed by the stationary Raman peaks remeasured after stored in air for 24 months (Figure S1h, Supporting Information).

The semimetallic nature of antimony permits a surface plasmon resonance at the interface between the AQDs and the dielectric medium. The imaginary part of the dielectric constant of antimony is much larger than that of Au and Ag (Figure 1f and Figure S8, Supporting Information), leading to stronger photoinduced surface plasmon generation, which is collective electron charge oscillations in metallic nanoparticles excited by incident light of certain spectrum region. For the AQDs, the surface plasmon is highly localized by the quantum dot size, as verified by the optical absorption of AQDs suspended in NMP in Figure 1g. The peak at $\approx$300 nm comes from intrinsically interband transitions of semimetal antimony, and the broadband absorption ranging from 300 to 1100 nm is attributed to the LSPR of AQDs.[14] When AQDs are stimulated by light, the surface conduction electrons oscillate with the electric field of light. In the electrostatic approach, the induced dipole electric field in spherical AQDs is proportional to $[\varepsilon(\omega) - \varepsilon_m]/[\varepsilon(\omega) + 2\varepsilon_m]$, where $\varepsilon(\omega)$ and ε_m are the dielectric constant of AQDs and surrounding medium, respectively. At the specific wavelength λ (i.e., the optical frequency ω) when the condition Re$[\varepsilon(\omega)] = -2\varepsilon_m$ is met, the polarizability experiences a resonant enhancement, and the absorption and scattering of light are greatly enhanced. This is how the LSPR occurs, and much more energy will be transferred to conduction electrons in AQDs, leading to electron transitions from lower energy state to a higher energy state (hot electron). A detailed verification is given in Note S2 (Supporting Information).

2.2. SSPM of Suspended AQDs

When these freestanding, nanoscale, suspended AQDs in a 1-mm-thin cuvette were exposed to either weak CW or intense femtosecond laser (80 MHz, 100 fs) within the LSPR band of the AQDs (**Figure 2**a), a strong SSPM effect was observed with a set of concentric interference fringes formed in the far field (Figure 2b and Figure S3, Supporting Information, the setup design is given in the Experimental Section). The effect comes from a large phase shift of $2N\pi$ (N refers to the number
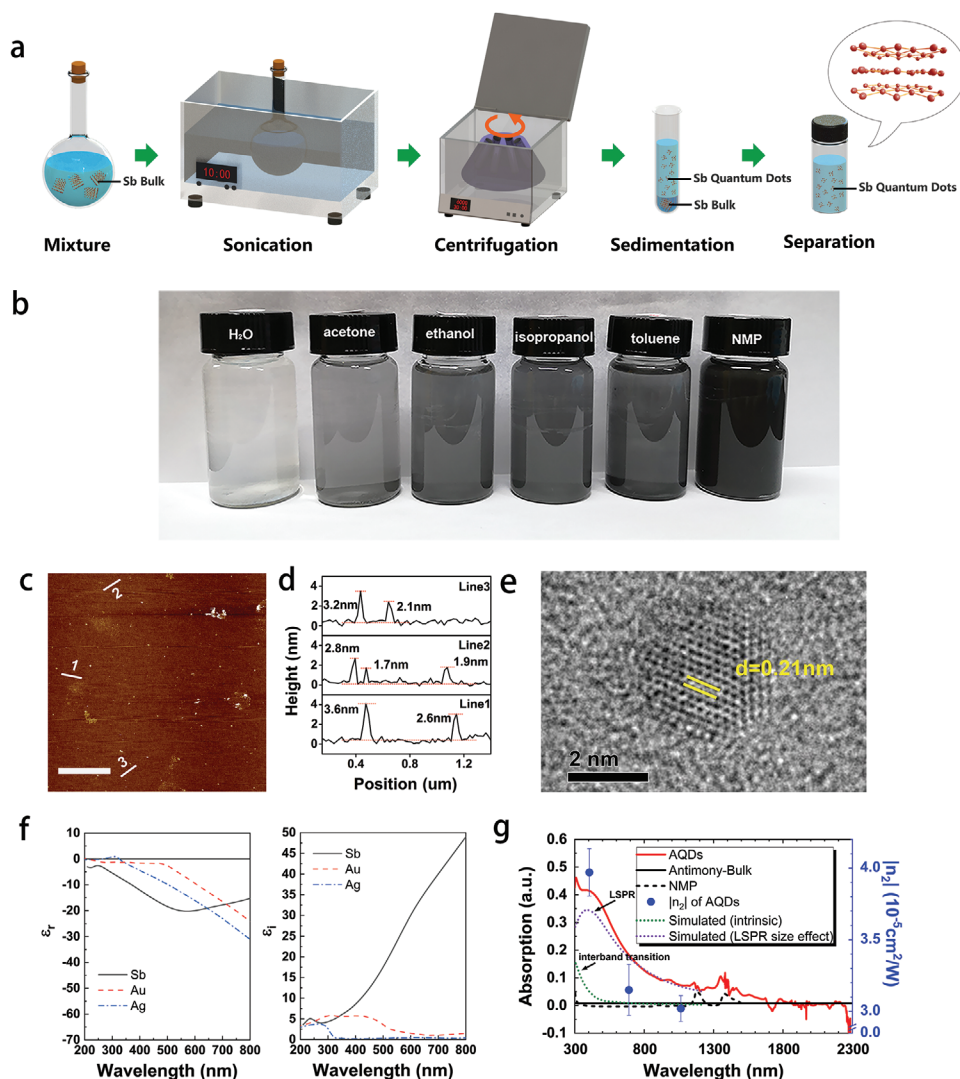
Figure 1. Preparation and characterization of AQDs. a) Procedure of liquid-phase exfoliation. b) AQDs in different dispersion media. c) AFM image of the AQDs on a thermally oxidized Si (300 nm SiO_2) substrate. d) Corresponding height distributions along the three white lines in (c). e) HRTEM image of a single quantum dot. f) Comparison of dielectric constant and imaginary parts among bulk Au, Ag, and Sb. g) Comparison of the absorption spectrum among AQDs in NMP (red solid), bulk antimony (black solid), and pure NMP solution (black dash). Blue circles: the calculated n_2 value of suspended AQDs from SSPM agreed with the absorption curve. The error bars are evaluated from the n_2 fitting. Dotted curves: Simulations on absorption based on FDTD (green) and Drude model (violet). In the Drude model, the plasmon frequency $\omega_p = 1.1 \times 10^{16}$ rad s^{-1} and the collision frequency $\gamma = 5 \times 10^{15}$ rad s^{-1}.

of diffraction rings) on the passed beams.[15] Interestingly, as shown in Figure 2c, the variations in the ring number of the CW and femtosecond lasers with the same average intensity are approximately the same, even though their peak intensities differ by 10^5. This strong dependence on the average intensity clearly indicates that the SSPM nonlinear response does not come from the intrinsic third-order dielectric susceptibility $\chi^{(3)}$ of the AQDs, as discussed in previous SSPM studies of suspended nanomaterials,[5] but originates from a clear manifestation of thermal-induced optical nonlinearity.[16] The fitting of the data in Figure 2c yields an effective nonlinear refractive index n_2 of 3.97×10^{-5} cm^2 W^{-1} (Note S2, Supporting Information), which is larger than most reported 2D nanomaterials (a specific comparison is presented in Table S1, Supporting

Information). This strong thermo-optic effect is attributed to plasmon-induced resonant energy transfer (PIRET), in which plasmonic energy can cross the metal/insulator interface by electron–phonon scattering (Figure 2d).[17] PIRET is a nonradiative process, in which hot electrons decay through electron–phonon scattering across the AQD/solvent interface, generating a large amount of heat and causing an extreme temperature rise in nearby local mediums or environments.[18] Such a plasmon-assisted process and subsequent thermo-optic effect changed the local refractive index, forming a local refractive index gradient (RIG) field that is responsible for the large n_2 of the AQD suspension. Moreover, the PIRET of AQDs is important for the manipulation of high-intensity laser fields beyond the damage limitation of general solid-state materials.
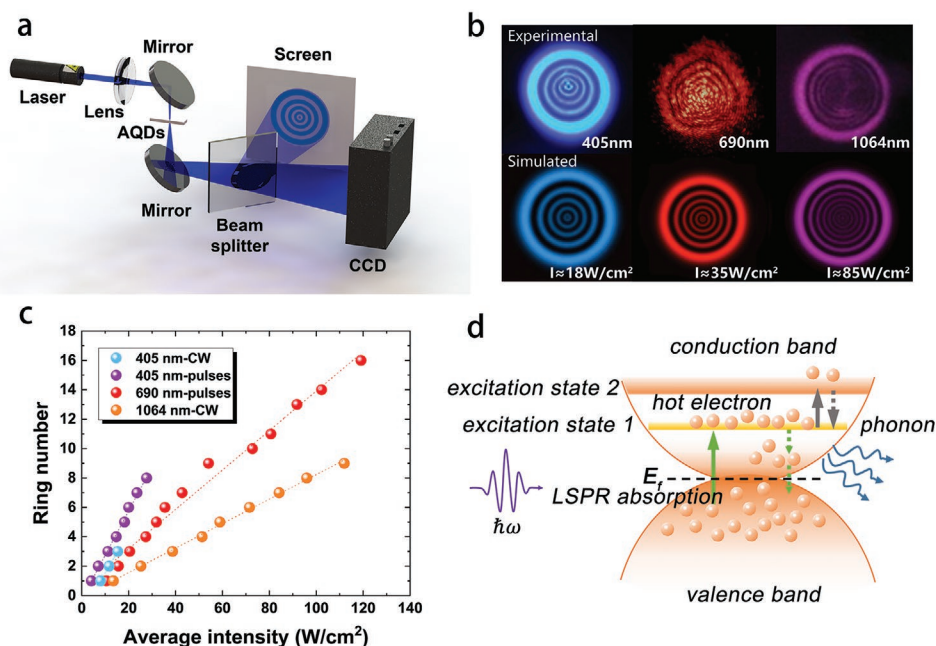
ADVANCED
SCIENCE NEWS
www.advancedsciencenews.com

ADVANCED
OPTICAL
MATERIALS
www.advopticalmat.de

Figure 2. Characterization of the n_2 of AQDs. a) Experimental setup for SSPM of AQDs. b) Top panels: SSPM diffraction ring patterns behind the AQD suspension. Bottom panels: numerical simulation with measured n_2. c) Dependence of the SSPM ring number on the laser intensity at different wavelengths. The straight lines are fitted by Equation (S2) (Supporting Information). The slopes are proportional to the effective nonlinear refractive index n_2. d) Dynamics of the PIRET by LSPR-assistant optical absorption and hot electron–photon scattering in AQDs.

2.3. All-Optical Modulation of Strong Light via Weak Light

AQDs have strong absorption and a large n_2 in the visible (VIS) spectral region, as well as weak absorption in the infrared (IR) region. This characteristic enabled us to perform a two-color all-optical switch via SXPM, in which one weak "modulation" beam can control the attenuation of a much stronger "signal" beam. The idea is to induce a thermal index gradient in the AQD suspension by a rather weak pump light lying in the efficient LSPR absorption region and passing the signal laser beam with a much stronger intensity but beyond the LSPR absorption region through the AQD suspension simultaneously. The spatial phase shift should completely depend on the strength of the weak beam, i.e., the n_2 change coming from the weak pump will lead to the "ON/OFF" alternation of the strong signal in the AQD suspension. Although a similar light-control-light design has been experimentally performed in MoS_2, SnS, and WSe_2 suspensions to date, the intensities of the signal beams are all lower than those of the pump beams and the spectral regions are limited to VIS and NIR (<1.0 μm).

Figure 3a depicts the process of this weak-control-strong and the corresponding setup. We used a dichroic beamsplitter to combine a weak ultraviolet (UV) pump laser beam and a strong IR signal laser beam and let the two beams pass through the cuvette containing the AQD suspension, with their propagation paths as close as possible. Without the UV pump light, the IR laser directly passed through the AQDs. When the UV laser illuminated the AQDs, strong LSPR excited electrons transitioned from the valence band to the conduction band. Then, the excited hot electrons relaxed to the ground state, releasing phonons and generating a large amount of heat. The following thermo-optic effect changed

the local refractive index into a Gaussian-like distribution, and then changed the trajectory of the copropagating IR beam. The IR beam diverged due to the low refractive index at the center and gradually formed concentric interference rings in the far field. By changing the on/off status of the pump light, we can control the pattern of the transmitted signal light to obtain all-optical switching.

In the first, we verified the AOM design by conducting the control of a CW signal laser (at the wavelength of 2 μm and focused intensity $I_s = 33.75$ W cm^{-2}) via weaker CW modulation laser beam (at 405 nm and focused intensity $I_m = 3.56$ W cm^{-2}). As expected, the signal laser turned from a Gaussian pattern into a ring pattern as soon as turning on the modulation laser, with intensity ratio of 1:9.5 between the modulation and signal beams. The corresponding change of far-field patterns is recorded by commercial IR camera (Spiricon PY III-C-B, Ophir Co. Ltd.) as shown in Figure 3b(I). Higher ratio could be obtained subsequent to increasing the power of CW signal, but strong-field laser (>10 GW cm^{-2}) can be rarely achieved by CW laser, and hence, we tried to perform weak-control-strong femtosecond laser with strong peak intensity which would be expected to occur in steps. Different-wavelength and different-intensity femtosecond lasers (100 fs of pulse duration, 5 kHz of pulse repetition, 1.65, 2, and 2.3 μm central wavelengths focused to a spot diameter of 270 μm, intensity is listed in **Table 1**) chosen as signal beams and successively focused into suspension were controlled by the 405 nm CW laser (2.21 kW cm^{-2}) that complete "ON/OFF" switch on the spatial intensity was detected, as shown in Figure 3b(II–IV). The maximum intensity ratio was calculated to be 1.5×10^8. The time response of signal energy controlled by modulation beam was measured with oscilloscope, as depicted in Figure 3b. A
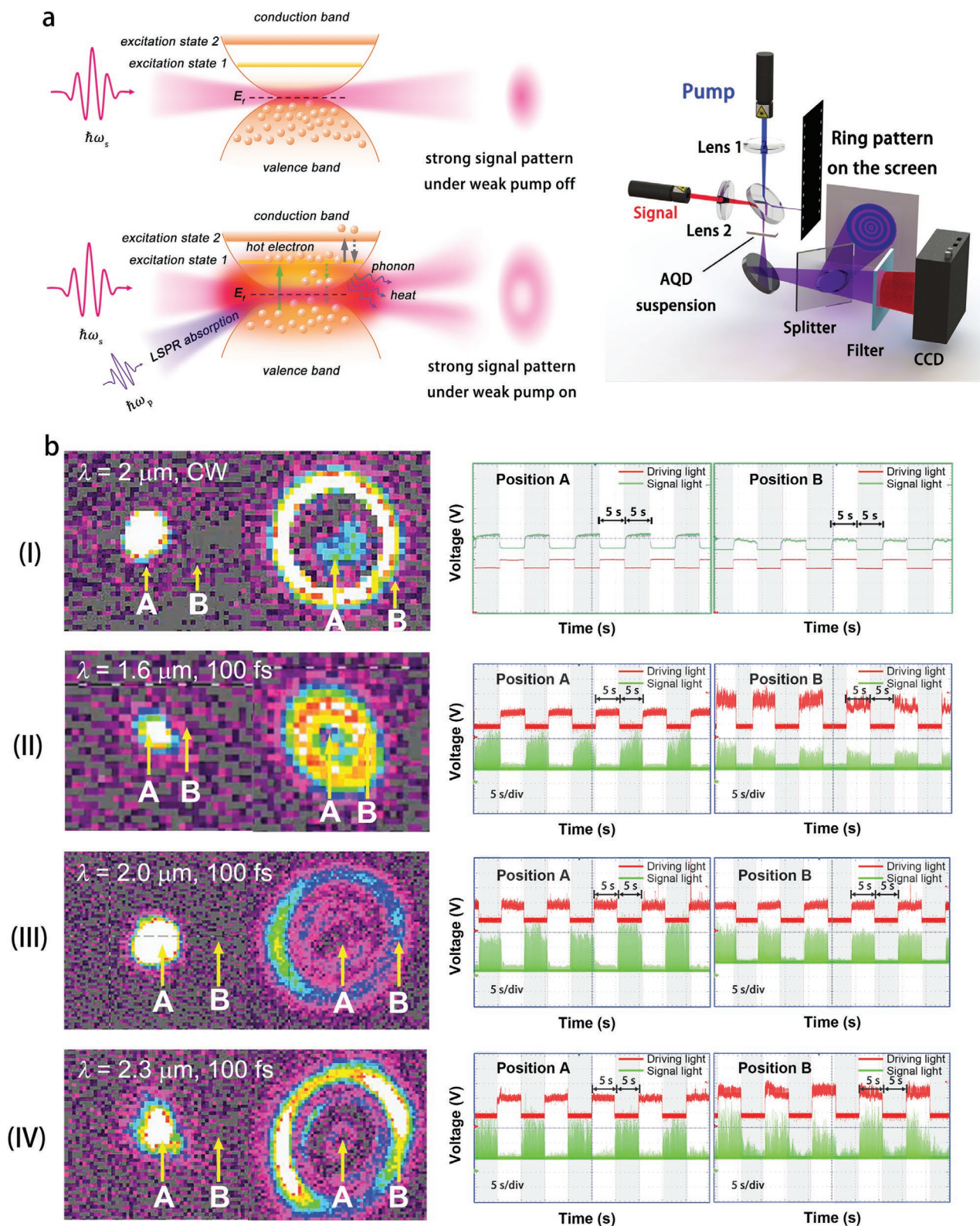
Figure 3. All-optical modulation of a strong laser via a weak laser based on the LSPR. a) Diagram of the all-optical modulation process. b) Left: far field patterns of the strong signal lasers for "ON" and "OFF" switching controlled by a 405 nm weak laser with different signal intensities (CW, femtosecond lasers) and wavelengths. Right: oscillograph curves for the corresponding temporal response of positions A and B, referring to the centers of the fundamental mode (FM) and first-order diffraction mode (FDM), respectively. Red curves: modulation laser. Green curves: signal laser. The ON/OFF interval is 5 s.

Table 1. Results of this AOM based on plasmon SXPM effect of AQDs.

Modulation light (wavelength, intensity)	Modulated light (wavelength, intensity)	Intensity ratio between modulation and signal beams
CW (405 nm, 3.6 W cm^{-2})	CW (2.0 µm, 33.8 W cm^{-2})	1:9.5
CW (405 nm, 2.2 kW cm^{-2})	100 fs (2.3 µm, 36.3 GW cm^{-2})	1:1.6 × 10^7
	100 fs (2.0 µm, 348.1 GW cm^{-2})	1:1.5 × 10^8
	100 fs (1.65 µm, 224.8 GW cm^{-2})	1:1.0 × 10^8
CW (405 nm, 48 W cm^{-2})	100 ps (3.0 µm, 8.7 kW cm^{-2})	1:1.8 × 10^2

nearly identical response was observed for multiple switching cycles, which demonstrates the robustness and reproducibility of our AOM. By contrast, no modulation is observed just using blank NMP (Figure S12, Supporting Information). In addition, to exploit MIR application, the switch of 100 ps pulses at 3 µm via CW laser was also performed under similar conditions with achieving an intensity ratio of 1:1.81 × 10^2 (Figure S4, Supporting Information). Broader operation bandwidth in MIR region is mainly restricted by the infrared absorption of carbonyl and oxhydryl in NMP. Transmission of NMP above 3.5 µm sharply declines. In order to get broader bandwidth, an oxygen-ion-free and low-toxicity solvent can be used to replace NMP, such as CH$_2$Cl$_2$. Over the course of applying femtosecond pulses of 348 GW cm^{-2} to the AOM, no noticeable ablation or sublimation of the sample was found at the focal region of the strong-field exposure, suggesting an ultrahigh damage threshold of AQDs compared with low-damage threshold of the conventional nanomaterials. We justify this superiority to the high-density surface plasmon and PIRET of AQDs that offers this AOM unique advantages in manipulating strong-field lasers. Compared with semiconductor, AQD, as a semimetal nanostructure, has much less skin depth that effectively avoids the damage induced by two-photon absorption, which is the primary damage mechanism for general semiconductor under high-power femtosecond laser with wavelength beyond its intrinsic absorption. Therefore, our AOM can endure a strong signal laser in IR region. The damage threshold is estimated to be about 2.7 TW cm^{-2} by using 2 µm femtosecond laser (100 fs, 5 kHz). As an additional aspect of the AOM, it is emphasized that the number of rings of signal lights depends on the signal light wavelength (Figures S5 and S6, Supporting Information). An intriguing strategy is proposed for wavelength measurements by coherent SXPM, which is an AQD-based mini-spectrometer (Note S3, Supporting Information). The results endow AQDs with potential applications in all-optical modulation, and make it possible to use weak driving light to control another laser with a much stronger (≈10^8) intensity in a broad spectral region, which benefits low energy consumption applications such as information transfer.[19]

2.4. Dynamical Response and Modulation Speed of the AOM

As described previously, LSPR-assisted SXPM supports a broadband AOM via weak excitation. A detailed understanding of the dynamic response of this AOM is necessary to fulfill the potential of our control system. Ultrafast transient absorption (TA) spectroscopy is a precise technique to investigate the dynamic process and the corresponding modulation speed of the AOMs.[20] We applied TA spectroscopy here (see the Experimental Section for details) to identify the dynamic response from hot electron generation to a solvothermal process and finally to the formation of the RIG field. As shown in **Figure 4**a, instantaneously after electron–hole pair generation in the AQDs, a fast light-transmittance change was unambiguously observed on a picosecond timescale. When the pump was a 400 nm fs laser and weak probe laser was swept across 400 to 750 nm, both overlapped with the LSPR band of the AQDs. Notably, the AQDs show significantly prolonged recovering edges than those of reported solid antimonene nanosheets,[21] indicating a more complex cross correlation of the pump and probe pulses relevant to the thermal distribution in a liquid. Therefore, the TA results of suspended AQDs should not simply be interpreted as common dual-exponential decaying, but are well fitted to a tri-exponentially decaying function (Figure 4b), as $\Delta T/T = y_0 + (a \cdot e^{-t/\tau_1} + b \cdot e^{-t/\tau_2} + c \cdot e^{-t/\tau_3})$. In this case, after the photon-excited interband transition, the establishment of plasmon's energy conversion process can be divided into three relaxation states as shown in Figure 4b,d. These states include the following: 1) a fast time constant (τ_1) ≈ 2 ps, referring to carrier–carrier intraband scattering and thermalization in the AQDs; 2) a following time constant (τ_2) ≈ 50 ps range, corresponding to hot electron cooling and recombination with a hole, accompanied by phonon scattering within the AQDs; and 3) a time constant (τ_3) ≈ 200 ps range, probably arising from phonon transfer across the AQDs/solution interface and thermal diffusion in the solution, forming a local refraction index gradient within the pump beam's radius of 384 µm, leading to the change in the pump power at the detector due to phase modulation. The four figures in Figure 4b draw the corresponding mechanism for the different states of the TA process. These ultrafast absorption dynamics confirm that the plasmonic effect of the AQDs plays an important role in the thermo-optical behavior, which is responsible for the photoexcitation intensity sensitivity as shown in Figure 4c. Notably, τ_3 is highly dependent on the exciting laser size. Based on previous reports on plasmonic thermal nonlinearity, the speed can be accelerated to <100 ps by concentrating the laser size to the diffraction limit, while it will decelerate for a larger laser size because of the limitation of the phonon diffusion velocity and phonon mean free path in the medium.[18c,22] It is reasonable to conclude that the suspended AQD system, adopting a fast LSPR photothermal nonlinearity localized at the hundreds of micrometers scale, represents a potential platform for exploring novel optical devices with miniature structures and fast optical modulation.

2.5. Mechanism of Plasmon-Enhanced Optical–Matter Interactions in AQD Suspension

Under AOM operation, an intense signal beam beyond the LSPR band is modulated simultaneously with RIG generation in the time regime τ_3. Hence, it is essential to distinguish the

**ADVANCED
SCIENCE NEWS**
www.advancedsciencenews.com

**ADVANCED
OPTICAL
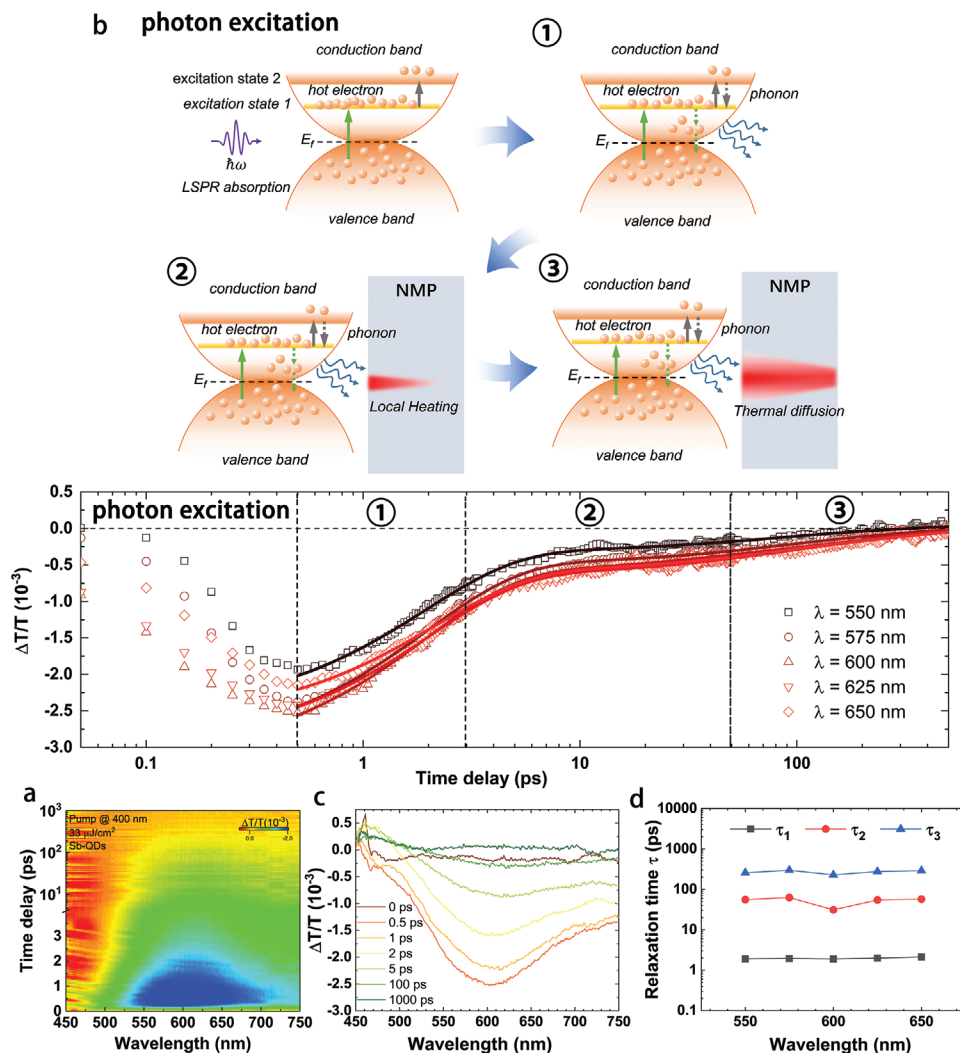MATERIALS**
www.advopticalmat.de

Figure 4. Photoexcitation transient dynamics of the PIRET in AQD suspension. a) TA spectra probed by the white-light supercontinuum under 400 nm resonant pumping. b) Bottom: Transient transmittivity plots at different typical wavelengths extracted from (a). Dots: experimental data. Solid line: tri-exponential decay fitting. The well-fitting demonstrates the presence of multiple decay states with different relaxation lifetimes marked as ①–③. Top figures: schematic mechanism for the decay states. c) TA spectra at different time delays pumped at 400 nm. d) Corresponding relaxation times after hot-carrier generation as a function of different probe wavelengths. The data were calculated by the tri-exponential fitting of (b).

transient evolution of the signal in τ_3 to determine the potential of the AOM. Unfortunately, it cannot be realized in experiments because the best commercial IR camera (Spiricon PY III-C-B, Ophir Co. Ltd.) that we can buy is only 30 FPS, which can only record the evolution of the signal at an interval of ≈30 ms, which is far longer than the value of τ_3. However, obvious ON/OFF modulation is visible between the first and second frames (Figure S9, Supporting Information), as clearly evident for the modulation occurring on a timescale faster than the camera recording. Here, we turn to investigating this evolution through simulation. The evolution process involves two steps: first, the photothermal conversion of AQDs in the incident weak pump laser; second, the thermo-optic effect of suspensions for a strong signal laser. A schematic of the photothermal conversion is shown in **Figure 5**a. As semimetal nanoparticles, the metallic property maintained in the AQDs enables an LSPR to

occur, and the nonradiative transition of resonant excited electrons facilitates local heating. A similar phenomenon has been utilized successfully for solar–thermal energy conversion.[23] Another reason contributing to photothermal conversion is the size effect of the quantum dots. The size of AQDs is smaller than the general mean free path of electrons, and the considerable boundary scattering of electrons occurs. Electron scattering is then followed by phonon-excitation and nonradiative decay processes, which generate extra heat. During the two photothermal conversion processes, the thermo-optic effect emerged synchronously. Heat produced by the AQDs diffuses into the surrounding medium, leading to a decrease in the refractive index due to the negative thermo-optical coefficient of NMP. Under irradiation of a Gaussian beam, the refractive index also exhibits a Gaussian distribution approximately on the cross section, as shown in Figure 5b (Figure S10 and
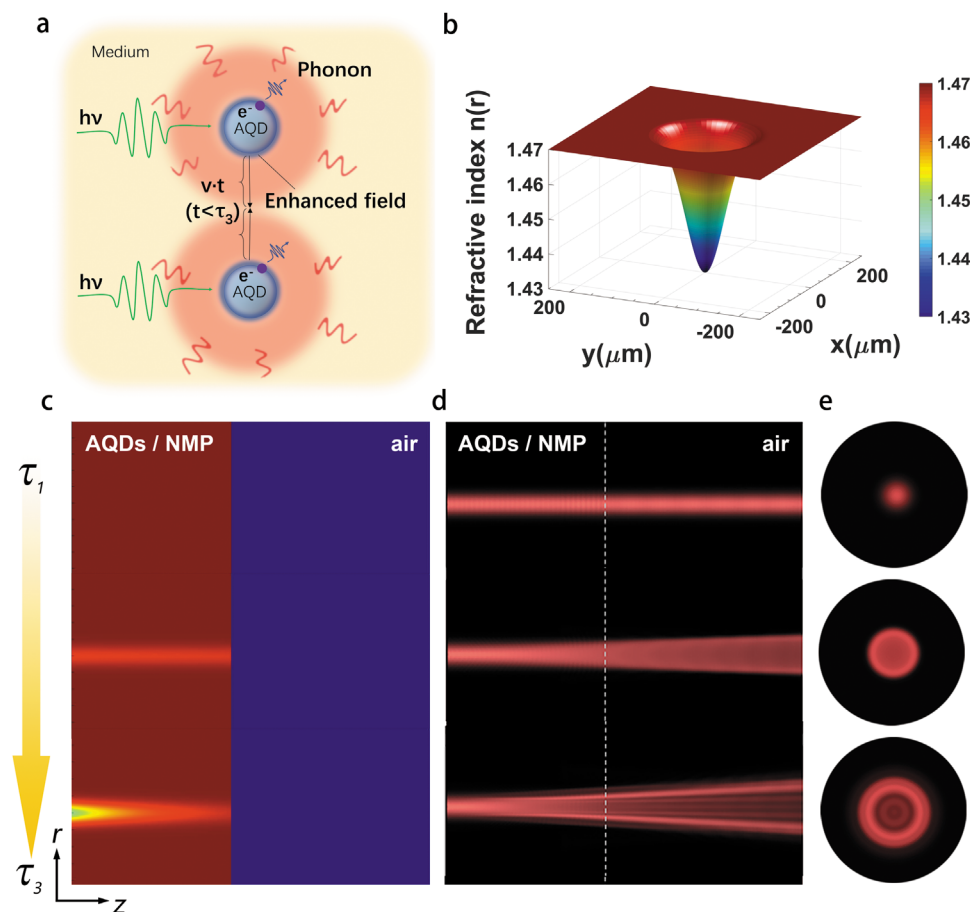
Figure 5. Analysis of the temporal evolution of the index gradient and spatial phase change for weak-control-strong-light interactions. a) Simple schematic diagram of the AQD suspensions. b) Refractive index profile changed by the thermo-optic effect. c) FDTD simulation for the temporal evolution of the refractive index field in AQD suspension simultaneously with the pump laser turning "ON" and d,e) kinetics of the thermo-optics.

Note S4, Supporting Information). Including the Lambert–Beer law for optical absorption, we deduced the refractive index distribution to

$$n(r,z) = n_0 \left(1 - \delta e^{-\frac{r^2}{w^2}} e^{-\alpha z} \right) \tag{1}$$

where δ is a coefficient proportional to the incident laser intensity I_0.[24] This distribution turned the initial beam into a divergent trajectory, and interference rings eventually formed in the far field. Actually, τ_3 measured above contained both the establishment and vanishment of the refractive index gradient, so the response time t is shorter than τ_3, as shown in Figure 5a.

The cross-sectional view displays the dynamics that the index transition region propagated throughout the whole thickness in the beam path direction, but the radial distribution shows a tendency for the refractive index to decrease from the center of the pump beam to its periphery. This trend implies that the volume of the all-optical device needed to trigger the switching is rather small and may be sub-millimeter sized. However, the shortest length of the cuvette that can be purchased is only 1 mm. We used FDTD simulations to demonstrate how the signal laser evolved along the propagation direction (Figure 5c). The effective nonlinear refractive index described by Equation (1)

accumulates a phase difference along the optical axis, resulting in the divergence of the light beam, and the intensity with the initial Gaussian distribution gradually turns into a saddle-shaped envelope, which forms interference rings in the far field. Distinct from the general thermal lens, the optical path difference along the radial direction here is much larger than one wavelength (Figure S2, Supporting Information), so that a tremendous phase gradient can lead to the formation of interference rings.

3. Conclusion

In summary, we experimentally demonstrated a design for an AOM covering the ultraviolet up to mid-infrared region (355 nm to 3.0 µm) based on plasmon-assisted thermo-optic nonlinearity in suspended AQDs. In such a device, a gate light reconfigured the phase distribution of a copropagating signal beam from the fundamental mode to diffraction rings by dynamically regulating the refractive index of the AQD suspension, leading to the "ON/OFF" alteration of the signal beam. This light–matter interaction had a strong strength even under rather weak CW laser excitation, derived from the enhanced broadband absorption of the localized SPR of semimetallic

AQDs. The interaction contributes a large effective nonlinear refractive index ($n_2 \approx 10^{-5}$ cm^2 W^{-1}) elaborately determined by SSPM. In addition, this switch can function as a new kind of facile and visual measurement on the signal central wavelength. Benefitting from the thermo-optical mechanism, refractive index changes hardly rely on the peak intensity, allowing for a strong pulsed laser modulated via weak light, which has never been achieved in general AOMs.

4. Experimental Section

Preparation of AQDs: AQDs were synthesized through a facile liquid-phase exfoliation method by using industrial antimony powder as the raw material. The suspension in a reagent bottle was sonicated in a bath uninterruptedly for 10 h at a power of 180 W. The resulting product was collected and centrifuged at 6000 rpm for 30 min. The final supernatant in NMP was irradiated by a 532 nm laser, where symmetrical Tyndall scattering was observed, verifying that it contained very small and uniform AQDs (Figure S1c, Supporting Information).

Transient Absorption Measurement: The TA was measured using a homemade femtosecond pump-probe system as reported previously.[25] The radii of the pump (400 nm pumped by 800 nm laser with a 1 kHz repetition rate and ≈90 fs duration time) and probe beams (supercontinuum light generated by 800 nm laser focus on a CaF$_2$ plate) overlapping within the AQD suspension sample were 384 and 200 μm, respectively.

SSPM Experiment with AQDs: To realize a small device volume appropriate for effective integration, the AQD suspension of 0.06 mg mL^{-1} in NMP was sealed into a compact cuvette (JGS1 quartz) with an optical length as short as 1 mm. All lasers (405 nm CW, 405 nm fs, 690 nm fs, 1064 nm CW) were focused vertically into the AQD suspension from a top convex lens with a 125 mm focal length. Vertical incidence is to avoid the collapse of diffraction rings during non-axis-symmetric thermal convection (Figure S11, Supporting Information).

All-Optical Modulation of Strong Light via Weak Light Experiment with AQDs: A 405 nm CW laser was focused into the AQD suspension vertically from a top convex lens with 125 mm focal length. The signal lasers were injected vertically by a convex lens of 75 mm focal length. The transmitted beams were split into two directions, one of which was collected on a white screen for direct observation, and the other was detected by a pyroelectric camera after filtering out the UV pump laser.

Supporting Information

Supporting Information is available from the Wiley Online Library or from the author.

Conflict of Interest

The authors declare no conflict of interest.

Author Contributions

J.X. and Z.Y. conceived the idea for the project. J.X. and C.Z. designed the experiments. Z.Y. and Y.H. provided the antimony sample. H.W. prepared the AQD samples and performed material morphology characterization. C.Z. performed the optical measurements and analyzed the data. C.Z. performed the numerical simulations. C.Z., J.X., H.W., and Z.Y. wrote the manuscript. All authors discussed the results and commented on the manuscript.

[1] a) N. Yoshikawa, T. Tamaya, K. Tanaka, *Science* **2017**, *356*, 736; b) Y. S. You, D. A. Reis, S. Ghimire, *Nat. Phys.* **2017**, *13*, 345; c) Q. Zheng, H. Zhu, S.-C. Chen, C. Tang, E. Ma, X. Chen, *Nat. Photonics* **2013**, *7*, 234; d) W. Chen, S. Bhaumik, S. A. Veldhuis, G. Xing, Q. Xu, M. Gratzel, S. Mhaisalkar, N. Mathews, T. C. Sum, *Nat. Commun.* **2017**, *8*, 15198; e) F. Krausz, M. Ivanov, *Rev. Mod. Phys.* **2009**, *81*, 163; f) P. B. Corkum, F. Krausz, *Nat. Phys.* **2007**, *3*, 381; g) A. A. Zozulya, S. A. Diddams, A. G. V. Engen, T. S. Clement, *Phys. Rev. Lett.* **1999**, *82*, 1430; h) P. B. Corkum, *Phys. Rev. Lett.* **1993**, *71*, 1994; i) S. Tokita, M. Hashida, S. Inoue, T. Nishoji, K. Otani, S. Sakabe, *Phys. Rev. Lett.* **2010**, *105*, 215004; j) T. Seifert, S. Jaiswal, U. Martens, J. Hannegan, L. Braun, P. Maldonado, F. Freimuth, A. Kronenberg, J. Henrizi, I. Radu, E. Beaurepaire, Y. Mokrousov, P. M. Oppeneer, M. Jourdan, G. Jakob, D. Turchinovich, L. M. Hayden, M. Wolf, M. Münzenberg, M. Kläui, T. Kampfrath, *Nat. Photonics* **2016**, *10*, 483; k) S. Kawata, H.-B. Sun, T. Tanaka, K. Takada, *Nature* **2001**, *412*, 697.

[2] a) Thorlabs Corporation, Free-Space Electro-Optic Modulators Specs, https://www.thorlabs.com/newgrouppage9.cfm?objectgroup_id=7559 (accessed: March 2020); b) Thorlabs Corporation, Liquid Crystal EO Amplitude Modulators Specs, https://www.thorlabs.com/newgrouppage9.cfm?objectgroup_id=2729 (accessed: March 2020).

[3] M. Taghinejad, W. Cai, *ACS Photonics* **2019**, *6*, 1082.

[4] a) J. C. Fernandez, D. C. Gautier, C. Huang, S. Palaniyappan, B. J. Albright, W. Bang, G. Dyer, A. Favalli, J. F. Hunter, J. Mendez, M. Roth, M. Swinhoe, P. A. Bradley, O. Deppert, M. Espy, K. Falk, N. Guler, C. Hamilton, B. M. Hegelich, D. Henzlova, K. D. Ianakiev, M. Iliev, R. P. Johnson, A. Kleinschmidt, A. S. Losko, E. McCary, M. Mocko, R. O. Nelson, R. Roycroft, M. A. Santiago Cordoba, V. A. Schanz, G. Schaumann, D. W. Schmidt, A. Sefkow, T. Shimada, T. N. Taddeucci, A. Tebartz, S. C. Vogel, E. Vold, G. A. Wurden, L. Yin, *Phys. Plasmas* **2017**, *24*, 056702; b) G. Lehmann, K. H. Spatschek, *Phys. Rev. E* **2019**, *100*, 033205; c) L. L. Yu, Y. Zhao, L. J. Qian, M. Chen, S. M. Weng, Z. M. Sheng, D. A. Jaroszynski, W. B. Mori, J. Zhang, *Nat. Commun.* **2016**, *7*, 11893.

[5] a) R. Wu, Y. Zhang, S. Yan, F. Bian, W. Wang, X. Bai, X. Lu, J. Zhao, E. Wang, *Nano Lett.* **2011**, *11*, 5159; b) G. Wang, S. Zhang, X. Zhang,

L. Zhang, Y. Cheng, D. Fox, H. Zhang, J. N. Coleman, W. J. Blau, J. Wang, *Photonics Res.* **2015**, *3*, A51; c) L. Miao, B. Shi, J. Yi, Y. Jiang, C. Zhao, S. Wen, *Sci. Rep.* **2017**, *7*, 3352.

[6] H. K. Tsang, C. S. Wong, T. K. Liang, I. E. Day, S. W. Roberts, A. Harpin, J. Drake, M. Asghari, *Appl. Phys. Lett.* **2002**, *80*, 416.

[7] L. Lu, W. Wang, L. Wu, X. Jiang, Y. Xiang, J. Li, D. Fan, H. Zhang, *ACS Photonics* **2017**, *4*, 2852.

[8] a) L. Wu, Y. Dong, J. Zhao, D. Ma, W. Huang, Y. Zhang, Y. Wang, X. Jiang, Y. Xiang, J. Li, Y. Feng, J. Xu, H. Zhang, *Adv. Mater.* **2019**, *31*, 1807981; b) L. Wu, W. Huang, Y. Wang, J. Zhao, D. Ma, Y. Xiang, J. Li, J. S. Ponraj, S. C. Dhanabalan, H. Zhang, *Adv. Funct. Mater.* **2019**, *29*, 1806346.

[9] a) Y. Song, Z. Liang, X. Jiang, Y. Chen, Z. Li, L. Lu, Y. Ge, K. Wang, J. Zheng, S. Lu, J. Ji, H. Zhang, *2D Mater.* **2017**, *4*, 045010; b) T. Xue, W. Liang, Y. Li, Y. Sun, Y. Xiang, Y. Zhang, Z. Dai, Y. Duo, L. Wu, K. Qi, B. N. Shivananju, L. Zhang, X. Cui, H. Zhang, Q. Bao, *Nat. Commun.* **2019**, *10*, 28; c) Y. Wang, W. Huang, C. Wang, J. Guo, F. Zhang, Y. Song, Y. Ge, L. Wu, J. Liu, J. Li, H. Zhang, *Laser Photonics Rev.* **2019**, *13*, 1800313.

[10] a) W. Tao, X. Ji, X. Xu, M. A. Islam, Z. Li, S. Chen, P. E. Saw, H. Zhang, Z. Bharwani, Z. Guo, J. Shi, O. C. Farokhzad, *Angew. Chem., Int. Ed.* **2017**, *56*, 11896; b) W. Tao, X. Ji, X. Xu, M. A. Islam, Z. Li, S. Chen, P. E. Saw, H. Zhang, Z. Bharwani, Z. Guo, J. Shi, O. C. Farokhzad, *Angew. Chem.* **2017**, *129*, 12058.

[11] L. Lu, X. Tang, R. Cao, L. Wu, Z. Li, G. Jing, B. Dong, S. Lu, Y. Li, Y. Xiang, J. Li, D. Fan, H. Zhang, *Adv. Opt. Mater.* **2017**, *5*, 1700301.

[12] a) P. Ares, F. Aguilar-Galindo, D. Rodriguez-San-Miguel, D. A. Aldave, S. Diaz-Tendero, M. Alcami, F. Martin, J. Gomez-Herrero, F. Zamora, *Adv. Mater.* **2016**, *28*, 6332; b) J. Ji, X. Song, J. Liu, Z. Yan, C. Huo, S. Zhang, M. Su, L. Liao, W. Wang, Z. Ni, Y. Hao, H. Zeng, *Nat. Commun.* **2016**, *7*, 13352.

[13] a) C. Lee, H. Yan, L. E. Brus, T. F. Heinz, J. Hone, S. Ryu, *ACS Nano* **2010**, *4*, 2695; b) H. Li, Q. Zhang, C. C. R. Yap, B. K. Tay, T. H. T. Edwin, A. Olivier, D. Baillargeat, *Adv. Funct. Mater.* **2012**, *22*, 1385.

[14] Z. Zhu, Y. Zou, W. Hu, Y. Li, Y. Gu, B. Cao, N. Guo, L. Wang, J. Song, S. Zhang, H. Gu, H. Zeng, *Adv. Funct. Mater.* **2016**, *26*, 1793.

[15] S. D. Durbin, S. M. Arakelian, Y. R. Shen, *Opt. Lett.* **1981**, *6*, 411.

[16] Y. Wang, Y. Tang, P. Cheng, X. Zhou, Z. Zhu, Z. Liu, D. Liu, Z. Wang, J. Bao, *Nanoscale* **2017**, *9*, 3547.

[17] a) J. Li, S. K. Cushing, F. Meng, T. R. Senty, A. D. Bristow, N. Wu, *Nat. Photonics* **2015**, *9*, 601; b) L. Zhou, X. Li, G. W. Ni, S. Zhu, J. Zhu, *Nat. Sci. Rev.* **2019**, *6*, 562.

[18] a) S. Mukherjee, F. Libisch, N. Large, O. Neumann, L. V. Brown, J. Cheng, J. B. Lassiter, E. A. Carter, P. Nordlander, N. J. Halas, *Nano Lett.* **2013**, *13*, 240; b) D. F. Swearer, H. Zhao, L. Zhou, C. Zhang, H. Robatjazi, J. M. P. Martirez, C. M. Krauter, S. Yazdi, M. J. McClain, E. Ringe, E. A. Carter, P. Nordlander, N. J. Halas, *Proc. Natl. Acad. Sci. USA* **2016**, *113*, 8916; c) M. L. Brongersma, N. J. Halas, P. Nordlander, *Nat. Nanotechnol.* **2015**, *10*, 25.

[19] a) Y. Shan, L. Wu, Y. Liao, J. Tang, X. Dai, Y. Xiang, *J. Mater. Chem. C* **2019**, *7*, 3811; b) Y. Jia, Y. Liao, L. Wu, Y. Shan, X. Dai, H. Cai, Y. Xiang, D. Fan, *Nanoscale* **2019**, *11*, 4515.

[20] a) K. F. MacDonald, Z. L. Sámson, M. I. Stockman, N. I. Zheludev, *Nat. Photonics* **2009**, *3*, 55; b) H. Baida, D. Mongin, D. Christofilos, G. Bachelier, A. Crut, P. Maioli, N. Del Fatti, F. Vallee, *Phys. Rev. Lett.* **2011**, *107*, 057402; c) K. Nozaki, T. Tanabe, A. Shinya, S. Matsuo, T. Sato, H. Taniyama, M. Notomi, *Nat. Photonics* **2010**, *4*, 477; d) M. R. Shcherbakov, P. P. Vabishchevich, A. S. Shorokhov, K. E. Chong, D. Y. Choi, I. Staude, A. E. Miroshnichenko, D. N. Neshev, A. A. Fedyanin, Y. S. Kivshar, *Nano Lett.* **2015**, *15*, 6985; e) M. Taghinejad, H. Taghinejad, Z. Xu, Y. Liu, S. P. Rodrigues, K. T. Lee, T. Lian, A. Adibi, W. Cai, *Adv. Mater.* **2018**, *30*, 1704915.

[21] F. Zhang, X. Jiang, Z. He, W. Liang, S. Xu, H. Zhang, *Opt. Mater.* **2019**, *95*, 109209.

[22] a) J. B. Khurgin, G. Sun, W. T. Chen, W. Y. Tsai, D. P. Tsai, *Sci. Rep.* **2016**, *5*, 17899; b) J. R. Adleman, D. A. Boyd, D. G. Goodwin, D. Psaltis, *Nano Lett.* **2009**, *9*, 4417.

[23] a) L. Zhou, Y. Tan, J. Wang, W. Xu, Y. Yuan, W. Cai, S. Zhu, J. Zhu, *Nat. Photonics* **2016**, *10*, 393; b) L. Zhou, Y. Tan, D. Ji, B. Zhu, P. Zhang, J. Xu, Q. Gan, Z. Yu, J. Zhu, *Sci. Adv.* **2016**, *2*, e1501227.

[24] C. Sheng, H. Liu, S. Zhu, D. A. Genov, *Sci. Rep.* **2015**, *5*, 8835.

[25] X. Huang, H. Li, C. Zhang, S. Tan, Z. Chen, L. Chen, Z. Lu, X. Wang, M. Xiao, *Nat. Commun.* **2019**, *10*, 1163.